Supporting Information for "Discussion of possible seismically triggered avalanches after the S1222a Marsquake and S1000a impact event"

Lucas A.[1], Daubar I. J.[2], Le Teuff M.[1], Perrin C.[3], Kawamura T.[1], Posiolova L.[4], Lognonn P.[1], Rodriguez S.[1], Giardini D.[5], Sainton G.[1], Mangeney A.[1], McEwen A.[6]

[1]Université Paris Cité, Institut de physique du globe de Paris, CNRS, F-75005, Paris, France
[2]Brown University, Providence, RI, USA
[3]Nantes Universit, Universit dAngers, Le Mans Universit, CNRS, UMR 6112, Laboratoire de Plantologie et Gosciences, UAR 3281, Observatoire des Sciences de lUnivers de Nantes Atlantique, Nantes, France
[4]Malin Space Science System, San Diego, CA, USA
[5]ETH, Zurich, Switzerland
[6]U. Arizona, USA

Contents of this file

1. Text S1 to S5
2. Figures S1 to S7

S1. Note on post-marsquake image request and mapping

Once the S1222a event were recorded and a estimate of the location was provided, we investigate the orbital image archive for checking if either this location were falling into a region showing specific surface features (tectonics or avalanche signatures). It appears that this fairly flat region showing a few impact craters, into which, dust avalanches were detectable (Fig. S1). We therefore initiate the mapping using CTX and HiRISE images in order to established the list of location of interest. Then we request to MRO's team to target those specific places.

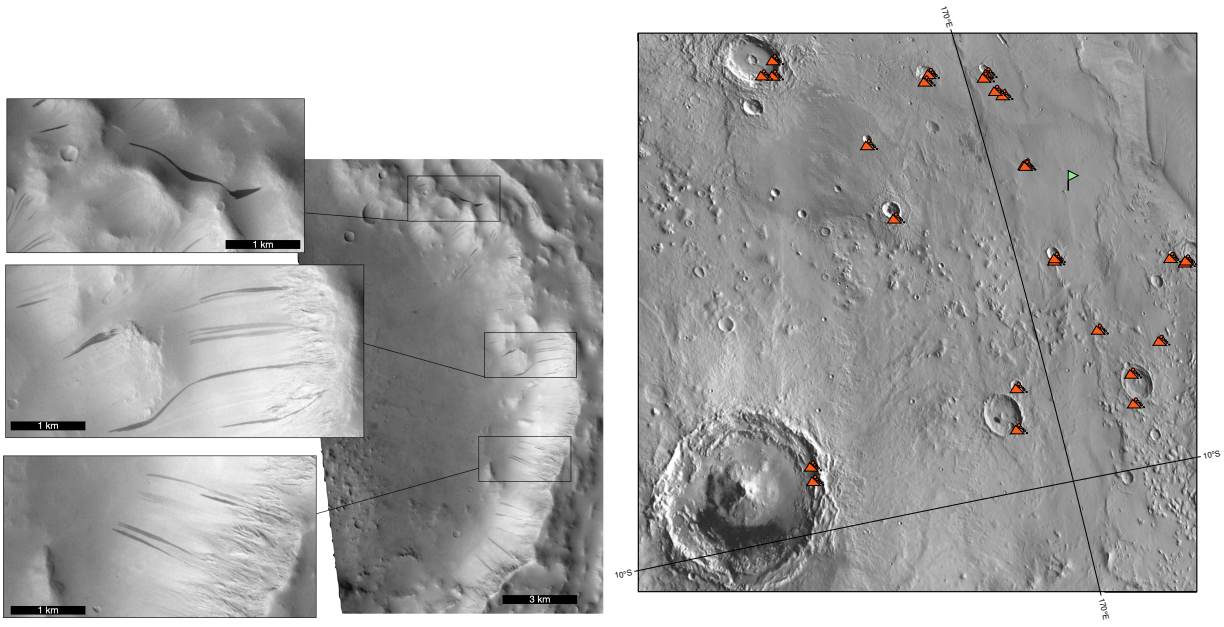

Figure S1. Location of the initial avalanche mapping once an estimate of the S1222a location was provided.

As we focus on maximising the temporal coverage, we utilized all released images from MOC, THEMIS-Vis, CTX and HiRISE sensors. This leads to various conditions of observation (i.e., emission angle, local time etc.) and hence large parallax effects, especially on steep slopes areas where avalanches occur (i.e., typically from 30 to 8 degrees). Consequently, the accuracy of the ortho-rectification performed with ISIS using either MOLA

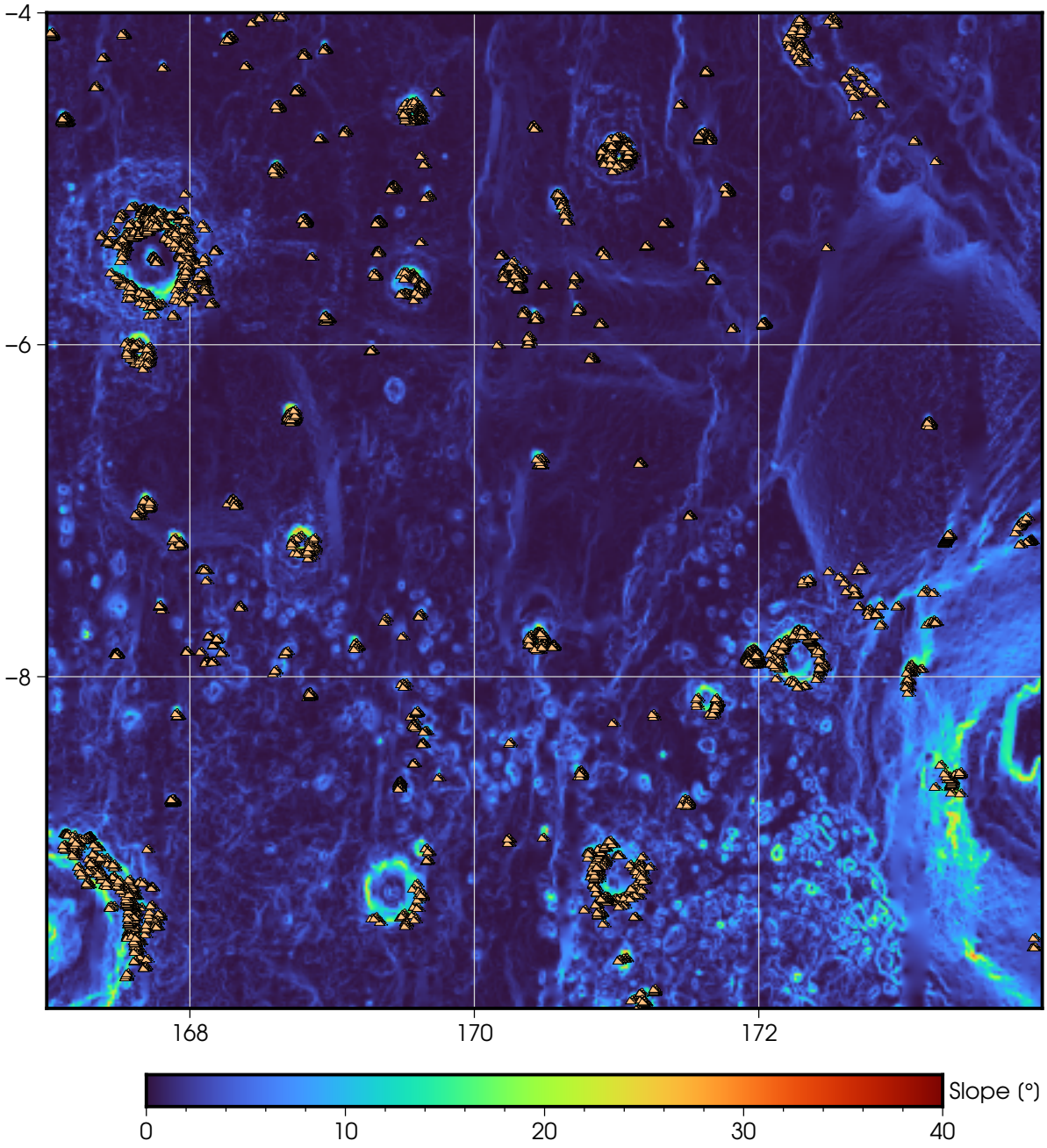

Figure S2. Slope map derived from MOLA 128ppd (Smith et al., 2001). Orange symbols show location of avalanches over the 2005-2021 period.

(Smith et al., 2001), and/or HRSC DTMs (Neukum & Jaumann, 2004), is not sufficient for accurate sub-pixel co-registration between all the images, even with bundle adjustment. This is an important aspect because as a result no automatic method could be used successfully (i.e., all of our principal component analysis (PCA) and Convolutional Neural Network (CNN) attempts failed to reach the required accuracy that could be achieved with human inspection). Hence we manually map all avalanches in the region shown in Fig. 1 in a Geographical Information System (GIS).

Then each pair of overlapping images (mostly CTX/CTX pairs, but we also considered CTX/HiRISE and HiRISE/HiRISE overlapping observations) leads to a detection of new (or absence of new) avalanches. This mapping work has been conducted by two independent people to compare and validate the results. Although non-MRO images offer a greater historical depth (∼15 Earth years), the resolutions are very different between

these sensors. Hence, over the 2008-2022 period, only CTX and HiRISE are considered. We down-sample the HiRISE data to 6 m/pixel, a pixel scale close to CTX's.

As well known, the brightness of these streaks is usually inversely proportional to their age. The darker they are, the more recently they formed (Sullivan et al., 2001). Note that we observe a very slow fading rate in this area, as some image pairs spanning 18 Earth years still show the same avalanches. Such a low fading rate allows us to estimate the long-term avalanche formation rate without concern that ongoing fading would significantly affect our measured rates (Aharonson et al., 2003). Additionally, this slow fading rate is in good agreement with the dust activity reported in this region (Battalio & Wang, 2021).

For the sake of comparison, the fading rate of dust devil tracks at the InSight landing site was also measured. There, dust devil tracks fade in a few months to almost two terrestrial years (Perrin et al., 2020). Notwithstanding, these are not formed by the same processes and thus might not fade at the same rates, in particular since avalanches remove a thicker layer of dust cover compared to dust devils. Other types of albedo features fade at different rates on Mars. For example, blast zones around new impacts have a median fading lifetime of 8 Mars years (Daubar et al., 2016), while dust devil tracks and rover tracks fade much more quickly as they remove dust more superficially (Balme et al., 2003; Verba et al., 2010; Geissler et al., 2010). To compare the same type of feature as studied here, other slope streaks have shown gradual fading over approximately 20 Mars years (e.g., Schorghofer et al., 2007; Bergonio et al., 2013).

S2. Note on the thermal inertia

The thermal inertia (Γ) is a complex data set that is not directly obtained from observations. Hence, there is no absolute value available. For instance, only apparent thermal inertia maps are derived from the THEMIS-IR camera (`https://astrogeology.usgs.gov/maps/mars-themis-derived-global-thermal-inertia-mosaic`). Because it is not a direct measurement, the properties is derived through models that have assumptions on many parameters. For instance, the radiative component is not considered in the distributed maps. Consequently, the thermal inertia is independent of the season and the local time, but no reference is provided. They also acknowledge that the temperature estimate is badly constrained, up to 180K according to Christensen et al. (2004). In figure S3, we show an example from our region of interest that exemplify this issue. First, we can see that Γ strongly differs over the swaths for the same terrains (Fig. S3-a). When looking at cross-section over the very same terrain, Γ is derived with almost 200 S.I. differences between orbits i.e., 400 S.I. vs 200 S.I. (Fig. S3-b). It results in more than 100% of discrepancies in the apparent value of the thermal inertia Γ. Consequently, depending on which swath is considered for scaling the qualitative map, we end up with very different results. Because we cannot have an absolute value over large areas, which is the case for our study, we therefore used the qualitative map provided as it offers a normalized (i.e. homogeneous) value over the planet.Then we scale this value using one swath from the quantitative apparent thermal inertia map and we end up with the values reported in the manuscript. In our case, we used the brighter swath (see Fig. S4), because it was the only swath not saturated in the harmonized map in regions where avalanches are observed.

To summarize, the absolute value is not important in this study as only relative values are important. Whatever the swath is considered for scaling Γ^*, the slope streaks are formed in the "relatively" higher values of the studied areas, as they formed on the steep slopes of craters as shown in Fig S5.

Note that Γ^* is equal to 440 S.I. in our homogenized map, while the value on the corresponding quantitative apparent map is 240 S.I. at avalanche's locations. The post-event avalanche rate is only higher compared to the pre-event rate, for the lowest Γ^* values. The distribution of the apparent thermal inertia remain similar for all avalanches through the period studied (Fig. S6).

a) b)

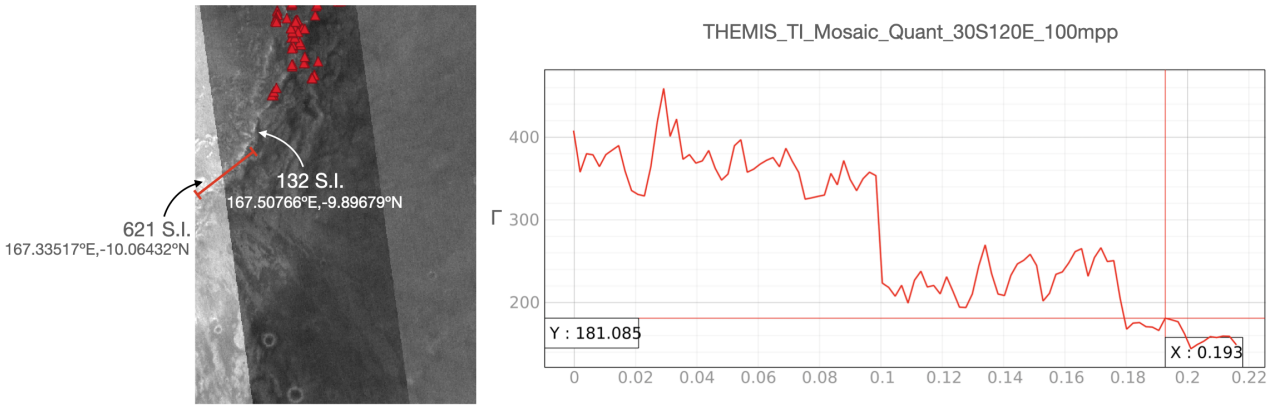

Figure S3. Example of discrepancies in the apparent thermal inertial between THEMIS-IR swaths. (a), close up on the quantitative apparent thermal inertial, centered at 167.50°E,9.89°S. The red transect is shown on panel b, where shifts of 180 S.I. are observed between swaths.

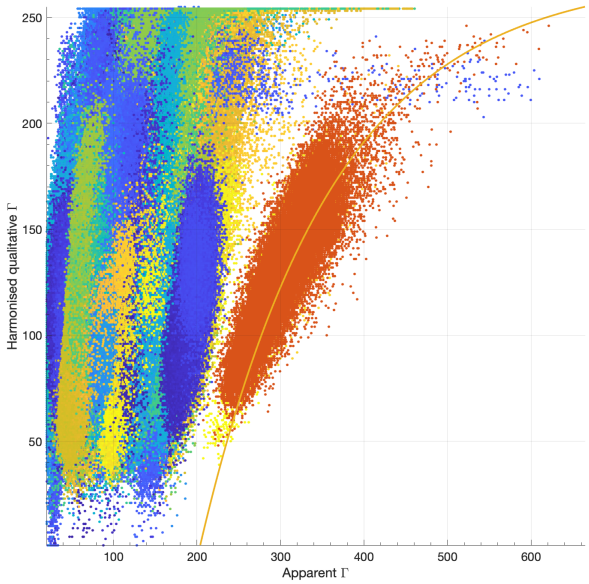

Figure S4. Relation between the apparent thermal inertia with the harmonized qualitative value. Colors scale with the different swath from THEMIS-IR. The red curve is the fit we used for converting the qualitative thermal inertial (8 bits) into an apparent thermal inertia expressed in S.I.

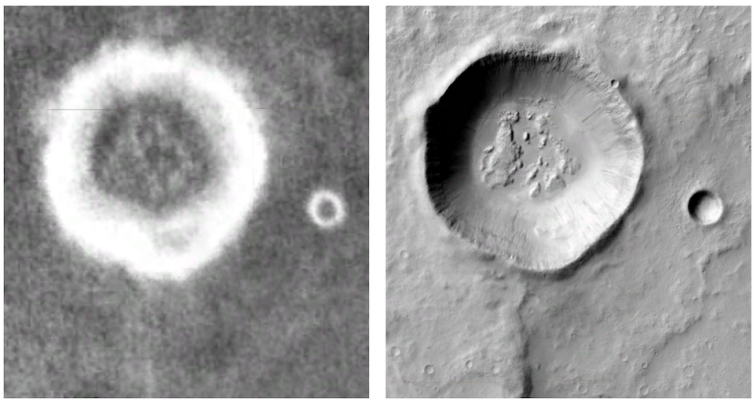

Figure S5. Example of thermal inertial map from THEMIS-IR with its visible counterpart from CTX over a crater showing dust avalanches.

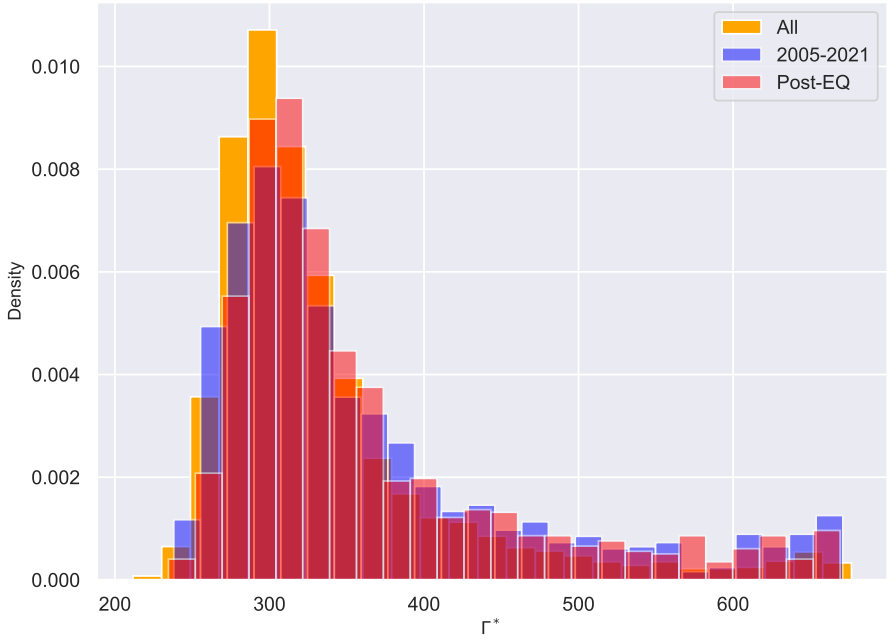

Figure S6. Distribution of the apparent thermal inertia Γ^*, as obtained from the empirical fit, over areas covered by avalanches over various periods.

S3. Note on the bootstrapping method

We can perform a hypothesis test to evaluate if the marsquake has a significant influence on the rate of avalanches. Here is the procedure:

Algorithm 1: Assessing Influence of marsquake on avalanche rate

Input: Pre-event image pairs $(n, \Delta n, \Delta t)$
Input: Post-event image pairs $(n, \Delta n, \Delta t)$

Define the observed test statistic: Δn_{obs} (change in the number of avalanches), n_{obs} (number of avalanches), and Δt_{obs} (time difference between images);

Combine the before and after data into a single pool, disregarding their original labels;

Perform resampling with replacement: Randomly sample, with replacement, from the pooled data to create a bootstrap sample of the same size as the original data set. Repeat this process to generate a large number of bootstrap samples.

Calculate the test statistic for each bootstrap sample: Compute the rate of avalanches for each bootstrap sample, given by $\frac{\Delta n_{boot}}{n_{boot}\Delta t_{boot}}$.;

Calculate the bootstrap statistic distribution: Collect the calculated test statistics from step 4 to form the bootstrap distribution of the test statistic;

Calculate the confidence interval: Determine the desired confidence level (e.g., 95%). Compute the lower and upper percentiles of the bootstrap distribution corresponding to the chosen confidence level;

Output: Assessment of marsquake influence

a) b)

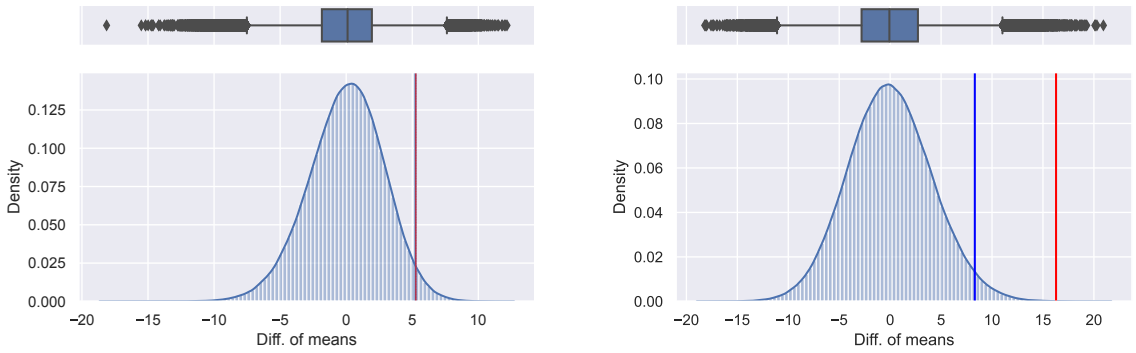

Figure S7. Bootstrapping statistics. (a) accounting for the whole data set, (b) when only considering q¿5 for the post-event observation. (top-panel) Quantiles of the permutation tests. (bottom-panel) The distribution of the permutation tests. The thin vertical blue lines gives the 95% of the test statistics distribution. The dashed red vertical line shows the observed statistics.

S4. Note on epicentral distance and ground deformation

Avalanche motion treated as a single-phase dry granular flow with Coulomb-type behaviour can be described by a two-dimensional Saint-Venant system. Hence, the transition between a static state and a flowing state is modelled by introducing a threshold allowing the material to flow. The friction forces $f(x, y, t)$ must satisfy

$$||f(x, y, t)|| \leq \mu\rho g h, \tag{1}$$

where μ is the friction coefficient, ρ the density, g acceleration due to the gravity, and h the thickness. This has been shown to quantitatively capture debris and rock avalanche morphodynamics on Mars (Lucas, 2010; Lucas & Mangeney, 2007; Lucas et al., 2011, 2014). Hence, this transition is sensitive to ground acceleration. The ground acceleration associated with an earthquake is generally evaluated through the PGA (Peak Ground Acceleration), the maximum amplitude recorded during an earthquake. On the zeroth-order, this value will depend on the epicentral distance. Following Gomberg, Felzer, and Brodsky (2006); Gomberg and Felzer (2008), we can relate the ground motion G with epicentral distance Δ through this simple relation:

$$PGA(\Delta) = \frac{K}{(\alpha + \Delta)^2}, \tag{2}$$

where K and α are empirical parameters (Gomberg & Felzer, 2008). Nonetheless, as on Earth, avalanches or rockfalls occur in response to a combination and cumulative forcings acting at different time scales including gravity, weathering and chemical effects, thermal, meteorological, seismic or volcanic activities (e.g. Tatard, 2010).

S5. Note on the inversion method and uncertainties

Following Mosegaard and Tarantola (1995), we can use inverse problem method to estimate what is the epicentral location that best explain the avalanche rate derived from orbital imagery.

As the "direct problem" consisting in predicting the d-values that we should observe when we make observations on a given system, such system can be described by a vector $\mathbf{m}$ of parameters, such as $\mathbf{m} = \{m_1, m_2, \ldots, m_i\}$. We can define a probability density $\sigma(\mathbf{m})$ that combines the a priori $\rho(\mathbf{m})$ information with the information provided by the experimental measurements (the data vector) and the information provided by the physics of the problem (i.e., the model). Hence, $\sigma(\mathbf{m})$ is called the posterior information. It is the combination of all the information we have and reads:

$$\sigma(\mathbf{m}) = k\rho(\mathbf{m})L(\mathbf{m}), \tag{3}$$

with k being a normalization constant (=1) and $L(\mathbf{m})$ the likelihood function accounting for a Laplacian experimental uncertainties, which reads:

$$L(\mathbf{m}) = \exp\left[-\sum_i \frac{\|G^i(\mathbf{m}) - d^i_{obs}\|}{\sigma_i},\right] \tag{4}$$

where $G^i(\mathbf{m})$ is the prediction by the model $\mathrm{G}(\mathbf{m})$ of the i^{th} observation, d^i_{obs} is the i^{th} observation with its associated uncertainties σ_i. In this study, the model $\mathrm{G}(\mathbf{m})$ is provided after Livio and Ferrario (2020) which relates the avalanche (or landslides in their paper) distribution with the epicentral distance Δ:

$$G(\mathbf{m}) = N_{ava} = a \exp\left[-\left(\frac{\Delta - b}{c}\right)^2\right], \tag{5}$$

where N_{ava} is the avalanches number triggered by the seismic event, where $\mathbf{m} = \{a, b, c\}$, with a the peak amplitude of the distribution, b the distribution peak distance to the epicenter, and c the distribution width. Hence, we randomly explore the longitude-latitude space (Lon $\in$ [166,175] and Lat $\in$ [-10,-1]) over 1 million runs. For each run, compute the epicentral distance for each avalanche's area that meet both conditions (Δt¡1.5 MYear and $\Gamma^* < 450$). Then, we fit the equation 5 on the observed N_{ava} vs Δ (expressed in euclidean distances and accounting for Mars flattening) using a non-linear least squares method. Finally, we compute the maximum likelihood function from equation 4 which accounts for a Laplacian distribution of uncertainties on the avalanche number.

The uncertainties on the avalanche rate q is computed after Aharonson et al. (2003), which reads:

$$\sigma = \left\langle \langle q - \langle q \rangle \rangle^{1/2} \right\rangle^2 = \frac{\langle q \rangle}{\sqrt{1 + \sum_i \Delta n_i}}, \tag{6}$$

with $\langle q \rangle$ being the expectation value of q, which reads:

$$\langle q \rangle = \frac{1 + \sum \Delta n_i}{\sum_i n_i \Delta t_i}. \tag{7}$$

References

Aharonson, O., Schorghofer, N., & Gerstell, M. F. (2003). Slope streak formation and dust deposition rates on Mars: Martian slope streak formation rates. *Journal of Geophysical Research: Planets*, *108*(E12). Retrieved 2022-07-14, from http://doi.wiley.com/10.1029/2003JE002123 doi: 10.1029/2003JE002123

Balme, M. R., Whelley, P. L., & Greeley, R. (2003). Mars: Dust devil track survey in argyre planitia and hellas basin. *Journal of Geophysical Research: Planets*, *108*(E8). doi: https://doi.org/10.1029/2003JE002096

Battalio, M., & Wang, H. (2021). The Mars Dust Activity Database (MDAD): A comprehensive statistical study of dust storm sequences. *Icarus*, *354*, 114059. Retrieved 2022-07-14, from https://linkinghub.elsevier.com/retrieve/pii/S001910352030405X doi: 10.1016/j.icarus.2020.114059

Bergonio, J. R., Rottas, K. M., & Schorghofer, N. (2013). Properties of martian slope streak populations. *Icarus*, *225*(1), 194-199. Retrieved from https://www.sciencedirect.com/science/article/pii/S0019103513001395 doi: https://doi.org/10.1016/j.icarus.2013.03.023

Christensen, P. R., Jakosky, B. M., Kieffer, H. H., Malin, M. C., Jr, H. Y. M., Nealson, K., ... Ravine, M. (2004). The thermal emission imaging system (themis) for the mars 2001 odyssey mission. In C. T. Russell (Ed.), *2001 mars odyssey* (pp. 85–130). Dordrecht: Springer Netherlands.

Daubar, I., Dundas, C., Byrne, S., Geissler, P., Bart, G., McEwen, A., ... Golombek, M. (2016). Changes in blast zone albedo patterns around new martian impact craters. *Icarus*, *267*, 86-105. doi: https://doi.org/10.1016/j.icarus.2015.11.032

Geissler, P. E., Sullivan, R., Golombek, M., Johnson, J. R., Herkenhoff, K., Bridges, N., ... Bell, J. (2010). Gone with the wind: Eolian erasure of the mars rover tracks. *Journal of Geophysical Research: Planets*, *115*(E7).

Gomberg, J., & Felzer, K. (2008). A model of earthquake triggering probabilities and application to dynamic deformations constrained by ground motion observations. *Journal of Geophysical Research: Solid Earth*, *113*(B10). Retrieved from https://agupubs.onlinelibrary.wiley.com/doi/abs/10.1029/2007JB005184 doi: https://doi.org/10.1029/2007JB005184

Gomberg, J., Felzer, K. R., & Brodsky, E. E. (2006). Earthquake dynamic triggering and ground motion scaling..

Livio, F., & Ferrario, M. F. (2020). Assessment of attenuation regressions for earthquake-triggered landslides in the italian apennines: insights from recent and historical events. *Landslides*, *17*(12), 2825-2836.

Lucas, A. (2010). *Dynamique des instabilités gravitaires par modélisation et télédétection: Applications aux exemples martiens* (Theses, Institut de physique du globe de paris - IPGP). Retrieved from https://tel.archives-ouvertes.fr/tel-00503212

Lucas, A., & Mangeney, A. (2007). Mobility and topographic effects for large valles marineris landslides on mars. *Geophysical Research Letters*, *34*(10).

Lucas, A., Mangeney, A., & Ampuero, J. P. (2014). Frictional velocity-weakening in landslides on earth and on other planetary bodies. *Nature Communications*, *5*(1), 3417.

Lucas, A., Mangeney, A., Mge, D., & Bouchut, F. (2011). Influence of the scar geometry on landslide dynamics and deposits: Application to martian landslides. *Journal of Geophysical Research: Planets*, *116*(E10).

Mosegaard, K., & Tarantola, A. (1995). Monte carlo sampling of solutions to inverse problems. *Journal of Geophysical Research: Solid Earth*, *100*(B7), 12431-12447. doi: https://doi.org/10.1029/94JB03097

Neukum, G., & Jaumann, R. (2004). The high resolution stereo camera of mars express. *ESA Special Publication*, *1240*, 1–19.

Perrin, C., Rodriguez, S., Jacob, A., Lucas, A., Spiga, A., Murdoch, N., ... Banerdt, W. B. (2020). Monitoring of dust devil tracks around the insight landing site, mars, and comparison with in situ atmospheric data. *Geophysical Research Letters*, *47*(10), e2020GL087234.

Schorghofer, N., Aharonson, O., Gerstell, M., & Tatsumi, L. (2007). Three decades of slope streak activity on mars. *Icarus*, *191*(1), 132-140. Retrieved from https://www.sciencedirect.com/science/article/pii/S0019103507001960 doi: https://doi.org/10.1016/j.icarus.2007.04.026

Smith, D. E., Zuber, M. T., Frey, H. V., Garvin, J. B., Head, J. W., Muhleman, D. O., ... Sun, X. (2001). Mars orbiter laser altimeter: Experiment summary after the first year of global mapping of mars. *Journal of Geophysical Research: Planets*, *106*(E10), 23689-23722.

Sullivan, R., Thomas, P., Veverka, J., Malin, M., & Edgett, K. S. (2001). Mass movement slope streaks imaged by the mars orbiter camera. *Journal of Geophysical Research: Planets*, *106*(E10), 23607-23633. doi: https://doi.org/10.1029/2000JE001296

Tatard, L. (2010). *Statistical analysis of triggered landslides : implications for earthquake and weather controls* (Unpublished doctoral dissertation). University of Canterbury and Universit de Grenoble.

Verba, C. A., Geissler, P. E., Titus, T. N., & Waller, D. (2010). Observations from the high resolution imaging science experiment (hirise): Martian dust devils in gusev and russell craters. *Journal of Geophysical Research: Planets*, *115*(E9).